Additive Manufacturing Letters 5 (2023) 100119

Contents lists available at ScienceDirect

Additive Manufacturing Letters

journal homepage: www.elsevier.com/locate/addlet

Short Communication

Tensile and creep-rupture response of additively manufactured nickel-based superalloy CM247LC

V. Kalyanasundaram[a], A. De Luca[a], R. Wróbel[a], J. Tang[a], S.R. Holdsworth[a], C. Leinenbach[a,b], E. Hosseini[a,*]

[a] Empa Swiss Federal Laboratories for Materials Science & Technology, Überlandstrasse 129, 8600 Dübendorf, Switzerland
[b] École Polytechnique Fédérale de Lausanne (EPFL), Laboratory for Photonic Materials and Characterization, Lausanne, Switzerland

ARTICLE INFO

Keywords:
Additive manufacturing
L-PBF CM247LC
Nickel superalloy
Tensile properties
Creep
Microstructure

ABSTRACT

Tensile and creep rupture properties of crack-free CM247LC alloy, processed via laser powder bed fusion, have been characterised in this work at temperatures up to 1000°C. The subject alloy matches or even exceeds the tensile performance of its directionally solidified counterpart up to 700°C, beyond which *both* the strength and ductility drop off relatively rapidly with increasing temperature. It was found that the agglomeration of discrete carbides – that essentially pin the grain boundaries – facilitate the nucleation, linking and propagation of micro-cracks along the adjacent grain boundaries at elevated temperatures. Relatively short-term creep-rupture tests conducted at 800°C show the need for greatly improving the microstructure of this alloy to compete with its directionally solidified or conventionally cast counterparts, especially considering that this material finds extensive application up to ~950°C in turbomachinery components. Increasing the grain size, incorporating grain boundary engineering concepts and a better understanding of carbide/γ' precipitate evolutionary characteristics can greatly help to improve the material's suboptimal creep response.

1. Introduction

Additive manufacturing (AM), and more particularly laser powder bed fusion (L-PBF), of high γ' volume fraction Ni-base superalloys remains challenging due to their elevated susceptibility to micro-cracking during fabrication [1–7]. Typically, three approaches are employed to address this critical issue in the AM of such alloys: (i) alloy design, (ii) process modification, and (iii) post-processing. The first strategy has the drawback to be quite time- and research-intensive, as it requires the development of custom-defined powder chemistries followed by a systematic characterisation of potential microstructural and mechanical property changes associated with each chemistry. For example, Griffiths et al. [7] demonstrated the possibility to build crack-free CM247LC parts by removing Hf from the alloy's composition. The size and chemistry of the γ' precipitates, carbides and borides were found to be notably modified after post-build heat treatment. Furthermore, considering the grain boundary strengthening effect imparted by Hf, mechanical properties at elevated temperature are expected to be adversely affected for the "No Hf" alloy variant.

Micro-crack mitigation by process modification includes strategies associated with preheating, scan strategy modification and melt pool control to name a few. As with that for alloy design, this approach too requires extensive evaluations as per a carefully constructed design-of-experiments optimisation routine. Among the process modification options, build-plate preheating especially comes with the disadvantage of requiring very high fabrication temperatures. As an example, Ramsperger et al. [5] fabricated crack-free CMSX-4 parts by electron beam-PBF with preheating above 1040°C. Similarly, preheating at 1200°C allowed the L-PBF fabrication of crack-free CM247LC parts [8]. This strategy is moreover difficult to be readily implemented in commercially available L-PBF machines. Alternatively, by adjusting consolidation parameters, Griffiths et al. [7] demonstrated that micro-crack density can be significantly decreased when consolidation of CM247LC is done in conduction mode as opposed to the keyhole or transition mode. While process modification can allow crack-free parts to be built, the processing window might be relatively small and potentially further reduced in parts with complex geometries.

Post-processing approaches such as hot isostatic pressing (HIP) have been shown to be highly effective in healing cracks after L-PBF fabrication of CM247LC-based alloys [1,9,10]. Most researchers view the consolidation of crack-free builds (with or without HIP) as only the first step in the production of γ' strengthened Ni-base superalloy parts

* Corresponding author.
E-mail address: ehsan.hosseini@empa.ch (E. Hosseini).

https://doi.org/10.1016/j.addlet.2022.100119
Received 17 November 2022; Received in revised form 12 December 2022; Accepted 29 December 2022

[3,11]. Attaining a preferred distribution (*i.e.* size, morphology and chemistry) of γ' precipitates needs an optimised post-process heat treatment (HT) strategy for nucleation and subsequent growth to the desired structures. Typically, a solutionising heat treatment is first conducted above the γ' solvus temperature to redissolve solute atoms and then an aging/precipitation hardening treatment at lower temperature(s) to obtain the desired distribution of γ' precipitates along with other carbides/borides [3,9,11]. Griffiths et al. [9] fabricated their "process-modified" CM247LC alloy with a tight control on powder chemistry and then subjected the material to HIP first followed by various HT conditions (both temperature and duration). They reported > 99.9% dense and crack-free material after HIP, along with an optimal distribution of γ' precipitates, carbides and borides after solutionising and aging HTs (HT details provided in *Section 2.1*).

Very little exists in the open literature concerning the high temperature performance of AM CM247LC alloy [9,12,13] especially considering that this alloy finds extensive application in turbomachinery components up to ~950°C. Interestingly, only one of these works [13] reported limited stress-rupture data with no information on the failure characterisation of the test specimens. In fact, a vast majority of existing literature on high γ' Ni-base superalloys processed via AM solely focus on aspects associated with crack-free builds and room temperature (RT) properties [14,15]. Here, we present an investigation of the room and high temperature (up to 1000°C) tensile properties of L-PBF CM247LC alloy as well as its creep-rupture response at 800°C. A detailed investigation of failure mode(s) – fractography and metallography – in the tensile and creep specimens has also been carried out, along with a discussion on the microstructural evolution characteristics for this alloy at elevated temperatures.

2. Experimental details

2.1. Test material and test matrix

The feedstock powder (Oerlikon Metco, Pfäffikon, Switzerland) used for the manufacture of the L-PBF CM247LC test blanks was obtained via inert-gas atomisation, with particles nominally ranging between 15–45 μm and a D_{50} percentile value of approximately 32 μm. The actual chemical composition of the powder is (in *wt.%*) 5.71% Al, 0.017% B, 0.06% C, 9.24% Co, 8.62% Cr, 0.02% Fe, 1.37% Hf, 0.54% Mo, 3.08% Ta, 0.73% Ti, 9.93% W, 0.006% Zr, 0.01% O and 60.67% Ni. A Sisma MySint 100 (Sisma S.p.A., Italy) L-PBF printer equipped with a 1070 nm fiber-laser operating in continuous wave mode with a Gaussian intensity distribution and a 55 μm spot diameter ($1/e^2$) was used for the fabrication of test blanks. The most important build process parameters were as follows: laser power of 175 W (7.35×10^6 W/cm^2), scan speed of 750 mm/s, hatch spacing of 75 μm and inter-layer thickness of 30 μm while adopting a bi-directional (90 degree rotation between layers) scan strategy. Blanks were built layer-by-layer perpendicular to the stainless steel base plate in the vertical direction (i.e. *z*-axis) so that the build direction was parallel to the loading direction during mechanical testing.

The as-printed specimen blanks first underwent HIP at 1225°C and 1000 bar for 5 h (Deloro Htm GmbH, Biel, Switzerland) followed by a solution HT at 1260°C for 2 h and then a precipitation hardening HT at 850°C for 8 h. Blanks were air cooled after each of the latter two heat treatment steps. The heat-treated blanks were then machined to the desired specimen geometries while ensuring that at least 1 mm thickness of material was removed from each side of the blanks. Standard dog-bone cylindrical specimens with a diameter of 4 mm and a parallel length of 12 mm were employed for the RT tensile tests. The diameter was reduced to 3 mm for the elevated temperature tensile and creep tests, keeping in mind the detrimental influence of high notch sensitivity (at transition radii) on ductility for AM CM247LC.

Three RT and two elevated temperature (ET) tensile tests each at 600°C, 700°C, 800°C and 1000°C were conducted at a strain-rate of 0.50% per minute in accordance with [16] and [17], respectively. Isothermal creep tests were conducted in accordance with [18] under four stress levels in the range 500-650 MPa at 800°C until specimen rupture. For the ET tests, three *K*-type thermocouples were equidistantly placed along the specimen gauge length and temperature was maintained to within ±1°C of the target value during the course of an entire test. It needs to be emphasised that these thermocouples were mechanically tied to the specimen surface and not spot-welded to potentially avoid premature crack initiation at weld spots. While thermal ramp-up for the ET tests took 1-2 hours, specimens underwent a further 30 minutes of soaking at the target temperature before the commencement of testing. A Class 0.5 side-entry extensometer, with a datum leg spacing of 10 mm, was used for the measurement and control of axial strain.

2.2. Failure characterisation

The fracture surface of all the failed creep-rupture specimens was first investigated under a FEI Quanta 650 Schottky field emission scanning electron microscope (SEM) to document both potential crack initiation site(s) and also the primitive fractographic characteristics. Based on these inputs, each specimen was sectioned parallel to the loading axis at a strategically chosen plane for further optical (metallographic) inspection. In addition, a few selected tensile test specimens were similarly sectioned for a more complete microstructural characterisation. The cut sections were hot-mounted in resin and then prepared as per standard protocol until polishing with 50 nm colloidal silica suspension. The samples were then chemically etched in V2A pickle (200 mL H_2O, 200 mL HCl 37%, 20 mL HNO_3 65% and 0.6 mL Sparbeize) at 60°C for 20 seconds and were optically inspected to reveal the macroscopic mode of primary/secondary crack propagation. It is important to note that this etchant preferentially attacks the "relatively" soft matrix, and leaves the precipitates/carbides and grain boundaries standing in relief. The etched specimens were investigated under the SEM again to further understand the microstructural evolution characteristics (precipitate/carbide coarsening) after exposure at elevated temperatures.

3. Results and discussion

3.1. Microstructure

Commonly used for high temperature applications, CM247LC superalloy contains an austenitic γ nickel matrix that is strengthened by the precipitation of (i) coherent and ordered intermetallic γ' precipitates within the matrix and (ii) blocky carbides primarily at grain boundaries aided by the inclusion of Hf. As compared to the grain structure in the as-fabricated state (see Fig. 1(a)), the microstructure of CM247LC after three heat treatment steps (i.e. HIP, solutionising and aging in that order) exhibited significant recrystallisation and grain growth (see Fig. 1(b)). The grains, however, were still more columnar than equiaxed with their orientation parallel to the build direction and were typically ~150–250 μm in width and ~750 μm to millimeters in length (mean values). Cuboidal shaped Ni_3(Al, Ti) γ' precipitates provide most of the strength for the alloy at elevated temperatures and were mostly formed during the cooling-down phase after solutionising. The γ' precipitates had a mean equivalent radius of 150-200 nm after solutionising and appeared to become finer (90 ± 37 nm) after ageing due to an inverse coarsening kinetic [9]. The discretely distributed carbides, rich in Ti/Hf/Ta/W/C, were 120 ± 57 nm in radii and provide additional strengthening to the material by effectively pinning down grain boundaries and their coarsening/sliding (see Fig. 1(c)). Quantitatively, the carbide area fraction was estimated via image analysis to be ~1.7%. Although the alloy in the as-built state exhibited notable elemental microsegregation, complete microstructural homogenisation was observed after solutionising [9]. Furthermore, investigation of the crack density distribution was not specifically conducted for the specimen blanks chosen for this study, considering they were built using the optimised conditions

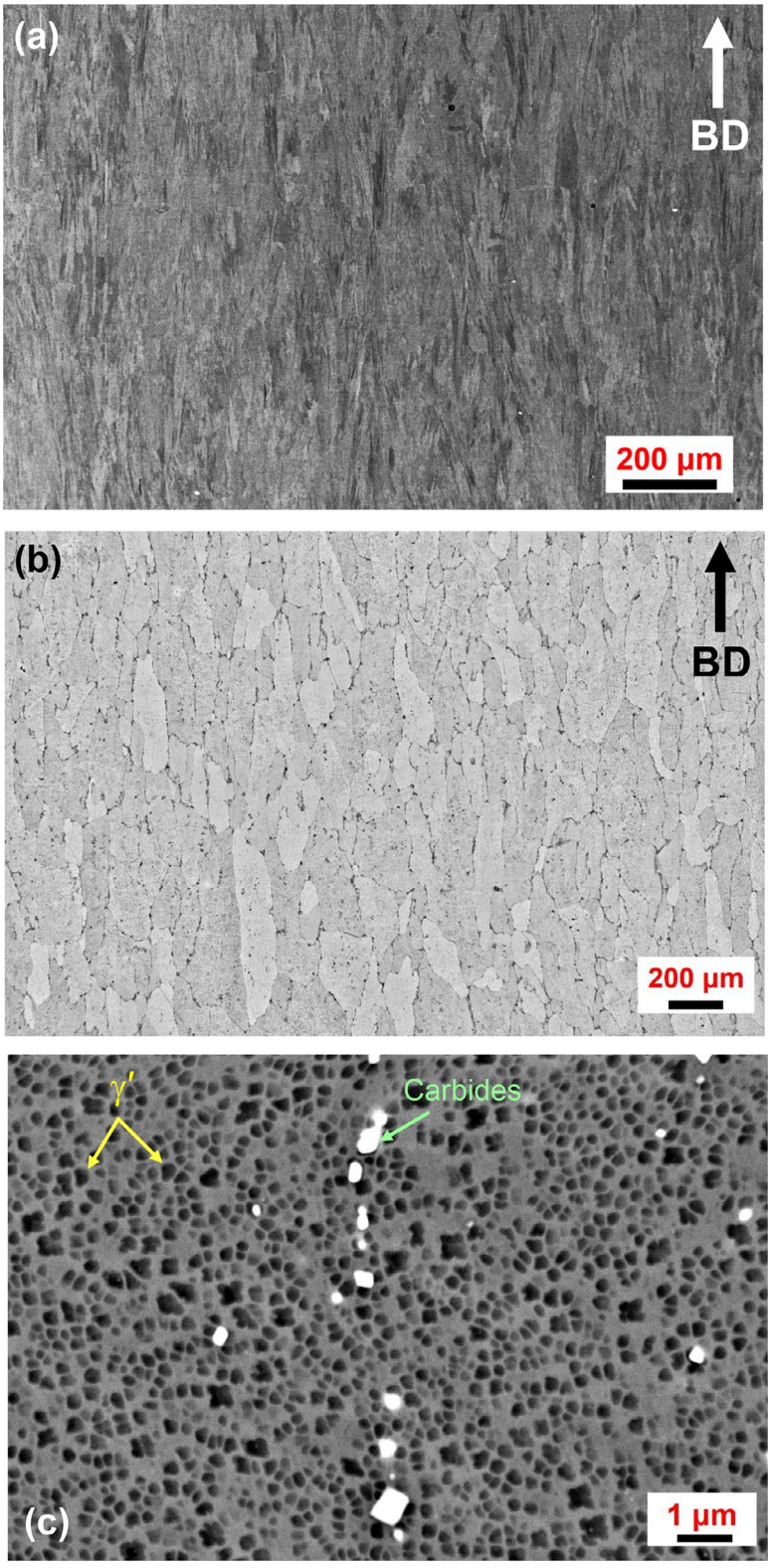

Fig. 1. Microstructure of L-PBF CM247LC material (a) in the as-fabricated state and (b) after the heat treatment considered in this work. BD stands for the build direction in both the micrographs. (c) High magnification scanning electron micrograph shows the typical distribution of γ' precipitates and blocky carbides after heat treatment.

to greatly minimise micro-cracking as detailed in our prior study [7]. Although randomly oriented intergranular microcracks were still observed in isolated locations, the blanks post-HIP were essentially crack-free with a < 0.10% mean area fraction of porosity. In summary, the size, amount and distribution characteristics of defects/cracks in post-HIP specimen blanks were deemed not so significant to warrant a more detailed evaluation (e.g. by X-ray Computer Tomography).

3.2. Tensile properties

Fig. 2(a) shows the 0.2% offset yield strength ($R_{p0.2\%}$) variation as a function of temperature for CM247LC processed via L-PBF, powder HIP, conventional casting and directional solidification (DS). It is necessary to point out here that only data from material that had seen one or more steps of heat treatment have been compiled in Fig. 2 to facil-

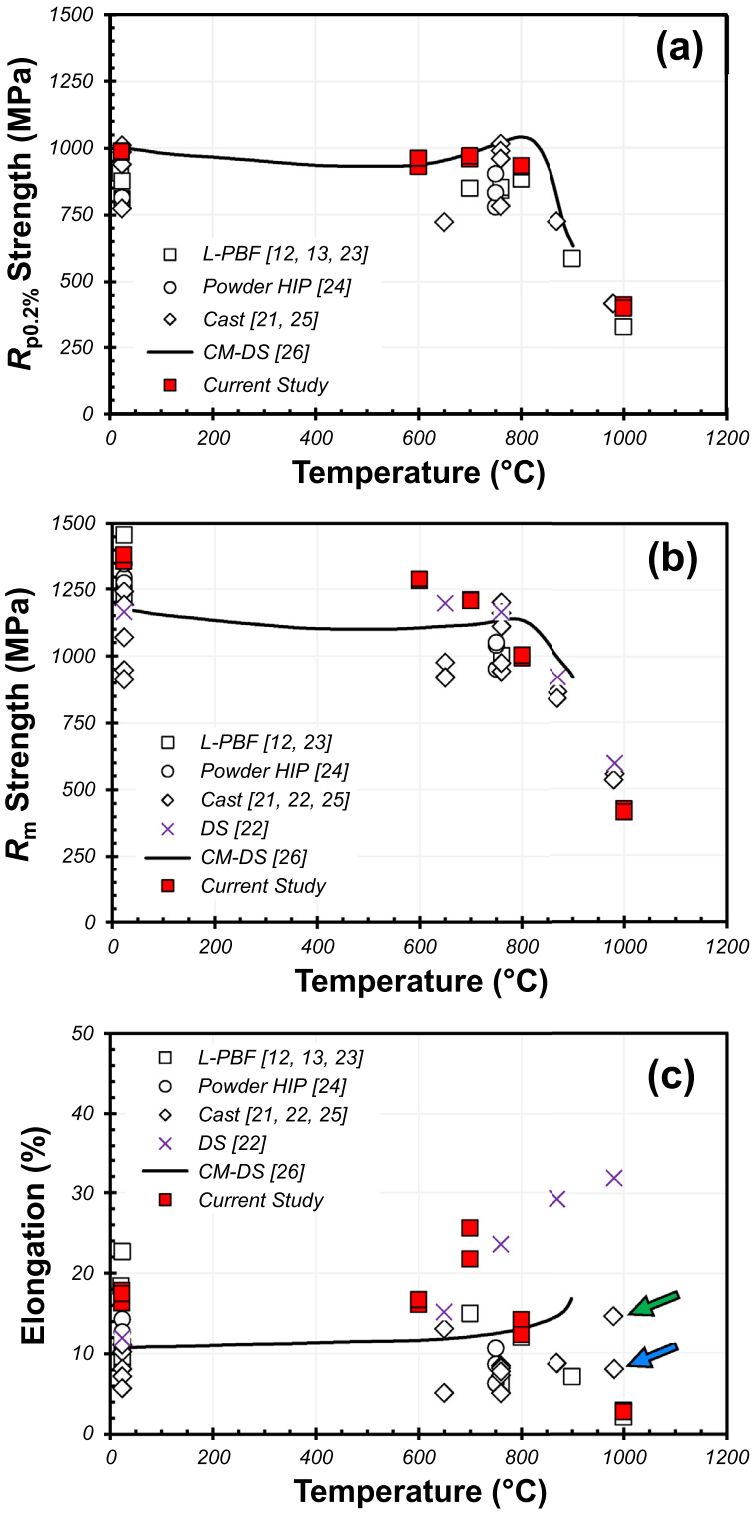

Fig. 2. Comparison of mechanical properties (a) 0.2% offset yield strength ($R_{p0.2\%}$), (b) tensile strength (R_m) and (c) tensile ductility as a function of temperature for the CM247LC alloy considered in this study, with those obtained for material processed via L-PBF [12,13,23] and other fabrication methodologies [21,22,24,25]. Open literature data [26] from the commercial supplier of the alloy, Cannon Muskegon, form the basis for the directional solidification trendline curves (CM-DS).

itate an equitable comparison, especially since L-PBF material in the as-fabricated state tends to offer an anisotropic material response along the build direction. Among the L-PBF batches, the proof strength was notably higher for the material considered in this work than its counterparts at all the test temperatures. Furthermore, the obtained flow stress was closely comparable to that of the DS material up to 700°C after which the L-PBF alloy appeared to soften while the DS alloy exhibits hardening until ~800°C. In this context, the anomalous yield behaviour of high γ' Ni superalloys is well documented in the literature [19,20] wherein the yield strength increases with increasing temperature from ~600°C and peaks between 700-800°C [21]. This phenomenon has been attributed to the enhanced strengthening achieved as a consequence of relatively lower dislocation mobility in this temperature range due to cross-slip kinetics. While the peak yield strength for the DS alloy is attained at ~800°C, it appeared to be closer to 700°C for the current L-PBF material. Above 800°C, the yield strength drops off quite precipitously and this softening has been explained on the basis of directional coarsening of γ' precipitates (*i.e.* rafting) in cast alloys [20,22]. The potential

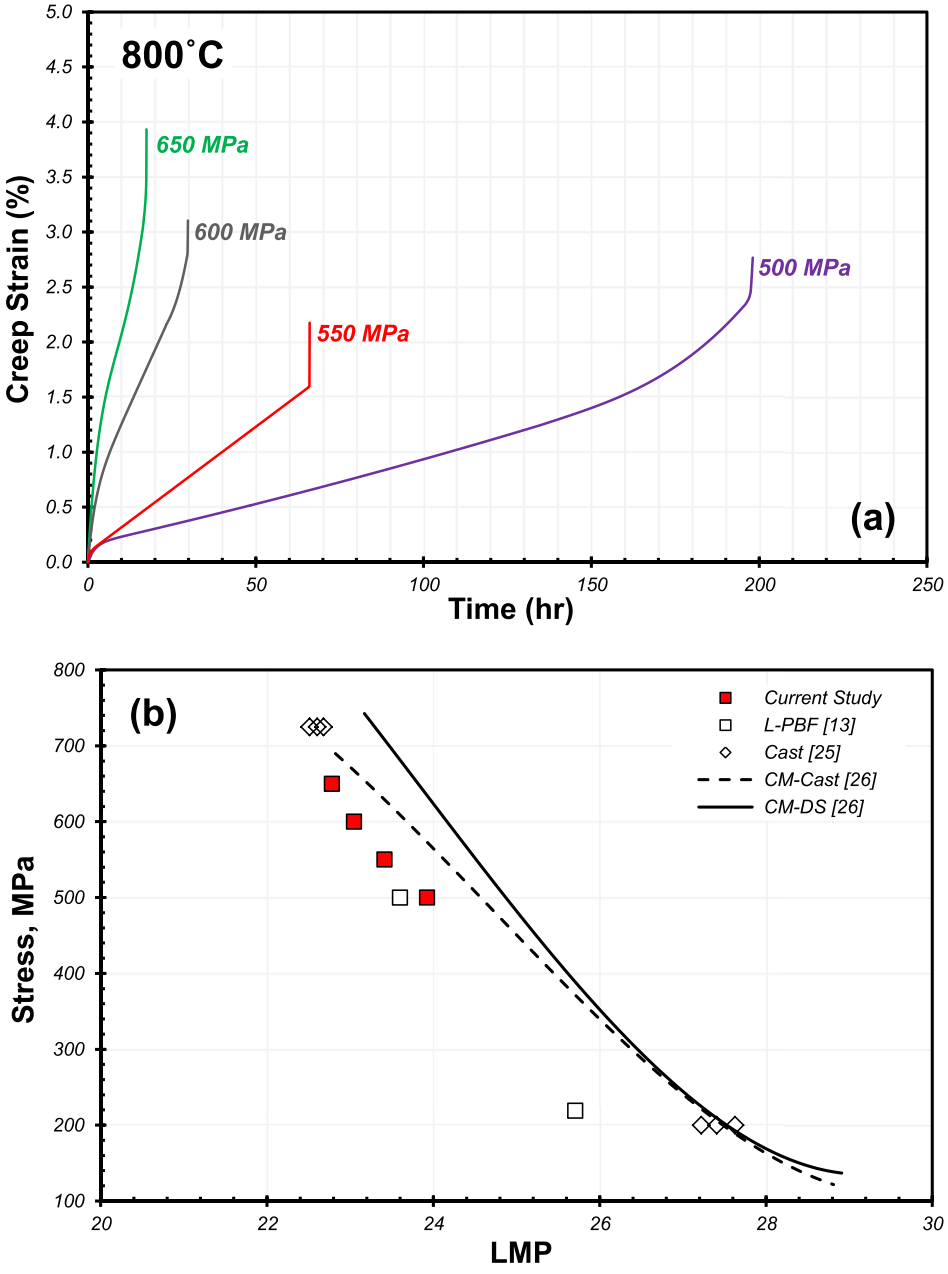

Fig. 3. (a) Isothermal creep deformation curves obtained for the considered CM247LC alloy at 800˚C and (b) comparison of creep-rupture lives determined at 800˚C in this work, with those obtained under various combinations of rupture time and temperature for the CM247LC alloy processed via L-PBF [13] and other fabrication methodologies [25]. Open literature data [26] from the commercial supplier of the alloy, Cannon Muskegon, form the basis for both the conventionally cast LMP trendline curve (CM-Cast) and the directional solidification LMP trendline curve (CM-DS).

reason(s) for rapid degradation in the strength of the current L-PBF alloy at ET are detailed in *Section 3.6*.

The variation of ultimate tensile strength (R_m) as a function of temperature for the CM247LC superalloy has been plotted in Fig. 2(b). The tensile strength decreased continuously with increasing temperature for the L-PBF alloy in this work, while the cast and DS alloys appear to exhibit a hardening trend qualitatively similar to that observed for yield strength at intermediate temperatures (albeit less pronounced). The test material also exhibited higher tensile strength than all its counterparts up to 700˚C except at room temperature as reported for another L-PBF alloy by Lee et al. [12]. The microstructure of the L-PBF alloy in [12] closely resembled that of the as-fabricated material since the only heat treatment step adopted – HIPing at 1200˚C – was well below the γ' solvus temperature. Considering that the test material in this work had much less of a columnar grain structure and also lower dislocation density (due to solutionising and recrystallisation above the γ' solvus) compared to that in [12], a slightly lower tensile strength at RT is certainly plausible. Although the extent of strain-hardening under tensile loading was found to decrease with increase in temperature, a notable drop in the hardening rate was observed for tests conducted at 800˚C and significantly more so at 1000˚C. Balikci et al. [27] reported strain-hardening in high γ' cast superalloys to be primarily governed by the size and morphology of precipitates; however, the influence of γ' precipitates on the weakening strain-hardening behaviour at ≥ 800˚C was found to be not as profound in the considered alloy, as discussed in *Section 3.6*.

The tensile elongation at fracture has been plotted in Fig. 2(c) as a function of temperature for the various product forms of CM247LC alloy. Keeping in line with the trends observed earlier for yield and tensile strength, the L-PBF alloy in this work exhibited much superior ductility (especially at ET) than its counterparts. Quite remarkably, peak ductility was observed at 700˚C wherein the peak "anomalous" yield strength was also attained. The elongation at fracture was comparable to that of the DS alloy at 800˚C beyond which the ductility dropped off quite considerably for the L-PBF alloy. A careful examination of all the ET tensile test specimens after fracture indicated negligible, if at all, localised deforma-

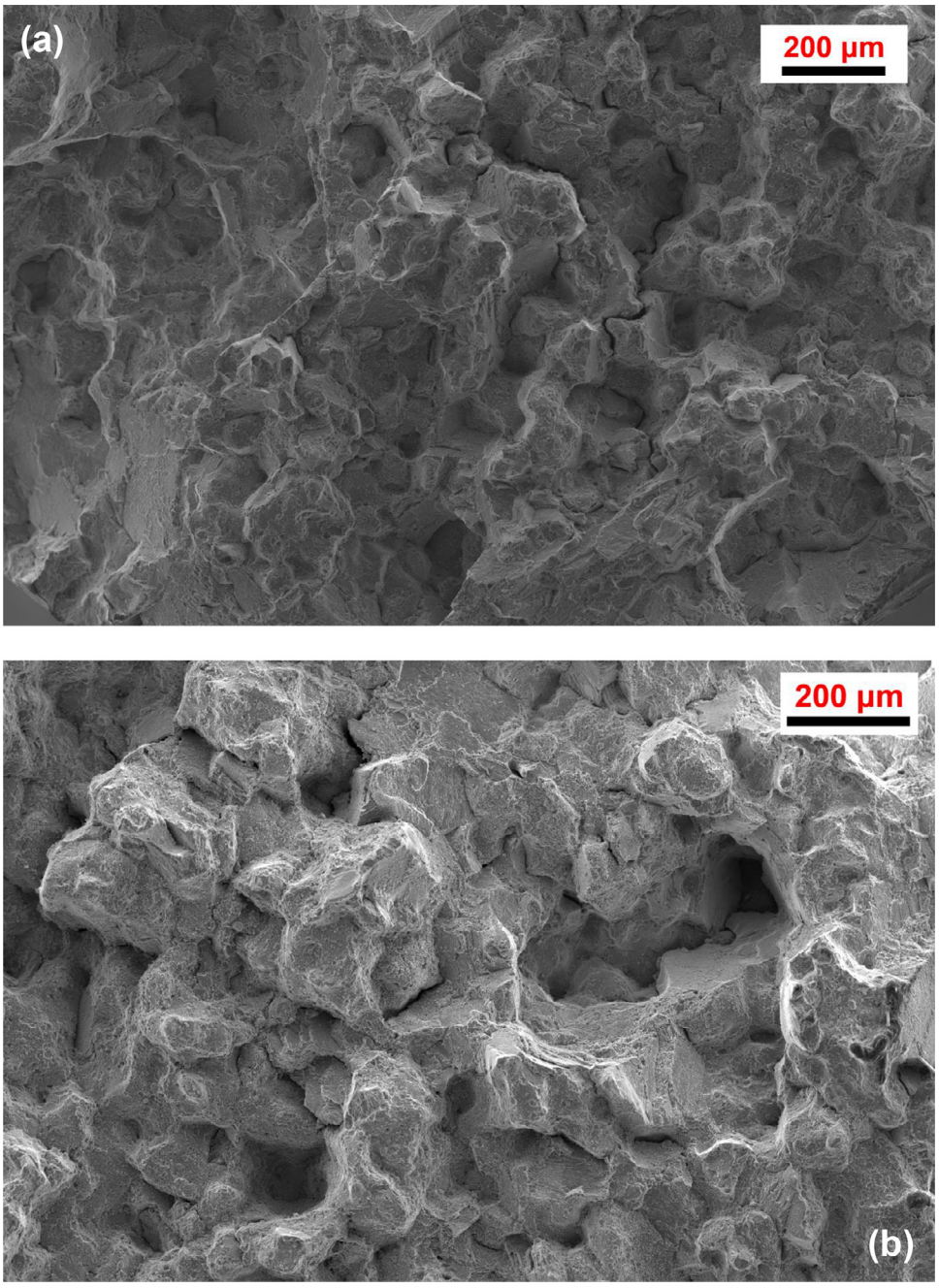

Fig. 4. Scanning electron micrographs of the fracture surfaces of L-PBF CM247LC alloy specimens creep tested at 800°C: (a) 650 MPa and (b) 500 MPa.

tion in the form of necking. This suggested that elongation in the parallel gauge length of test specimens was predominantly due to uniform deformation and was consistent with high strain-hardening observed until 700°C. At and above 800°C, higher ductilities could be expected considering the relative ease with which dislocations can move due to their enhanced thermal mobility along with lower (barrier) activation energy for motion. Tang et al. [13] and Ghoussoub et al. [28] observed grain boundaries to be the ductility limiting microstructural features in L-PBF CM247LC alloy at ET. Besides this, the reason for the drop-off in ductility at ≥ 800°C in this work could be explained, in part, by the agglomeration of carbides as detailed in *Section 3.6*. The role of carbides and their evolution at elevated temperature to this effect need a further systematic investigation.

The influence of other factors – like grain size and strain-rate – on monotonic mechanical properties of the CM247LC alloy certainly merits a discussion at this juncture. Huang and Koo [25] have shown that CM247LC casts perform relatively much better with decreasing grain size both in terms of strength (yield and ultimate) and ductility at RT and ET (760°C). They also observed the coarse-grained material to outlive the other two fine-grained variants in short-term creep tests at 982°C but still with relatively lower ductility. These results clearly point out to an inflection at ~700-800°C, as the performance of CM247LC casts is dictated by grain size below that temperature range, and by the microstructural degradation kinetics of γ' precipitates and carbides above that. Tailoring the microstructure of L-PBF alloys, in accordance with this observation from cast material, may thus be necessary for improving the elevated temperature ductility in particular.

Kim et al. [21,22] investigated the tensile properties of CM247LC cast material under two nominally different strain-rates (0.50% and 5% per minute) at 25-982°C. Although the strength variation was not materially different, tensile ductility particularly at 982°C was almost twice higher at the highest strain-rate than that at the lowest (indicated by a

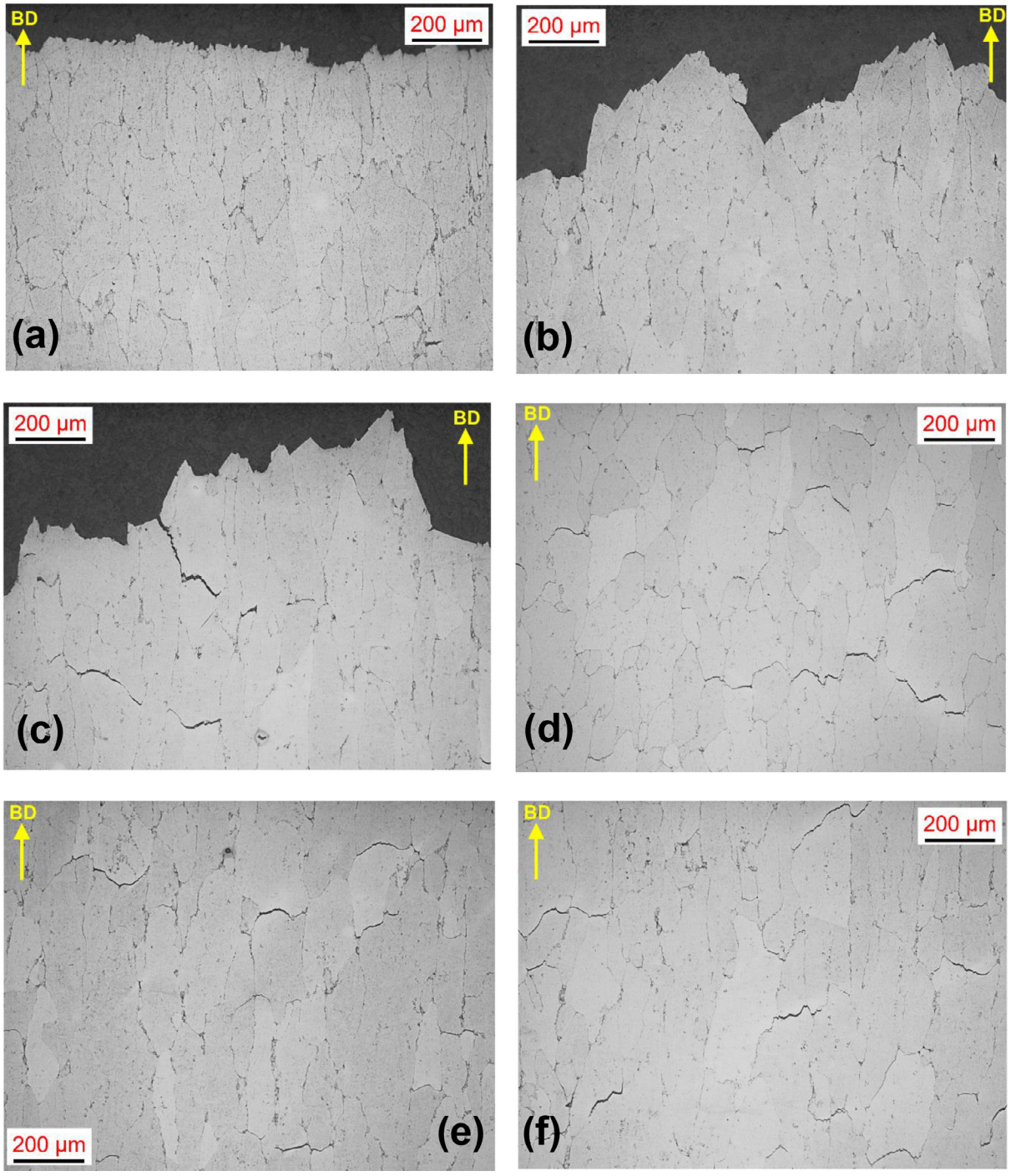

Fig. 5. Optical micrographs of the longitudinal cross-section of L-PBF CM247LC alloy specimens tensile tested at (a) RT, (b) 700°C, (c) 800°C and (d) 1000°C, and creep tested at (e) 800°C, 650 MPa and (f) 800°C, 500 MPa. BD in all the micrographs indicates the build direction.

green and blue arrow, respectively in Fig. 2(c)). The sensitivity of cast CM247LC alloy's ductility to strain-rate at elevated temperatures can thus be inferred, but the microstructural reason(s) for this material response are still unclear. Evaluating the influence of strain-rate on the tensile ductility of current L-PBF alloy is beyond the scope of the presented work and will be considered in future studies.

3.3. Creep properties

As discussed earlier, the peak "anomalous" yield strength of the considered L-PBF alloy was expected to be attained around 700°C. Although the strength values were comparable between the test material and DS alloy at this temperature, tensile ductility was markedly much higher for the former than the latter. In order to facilitate a better comparison, creep tests were instead conducted at 800°C where the tensile ductilities were similar without compromising too much on the strength. The evolution of creep strain over time for four stress levels at 800°C is shown in Fig. 3(a). As expected, the time to rupture increases with decreasing creep stress. Under all the test conditions, the test material displayed three distinct phases of creep deformation – primary, secondary and tertiary – with more time spent in secondary creep than the other two combined. Quite importantly, elongation at creep rupture (2-4%) was

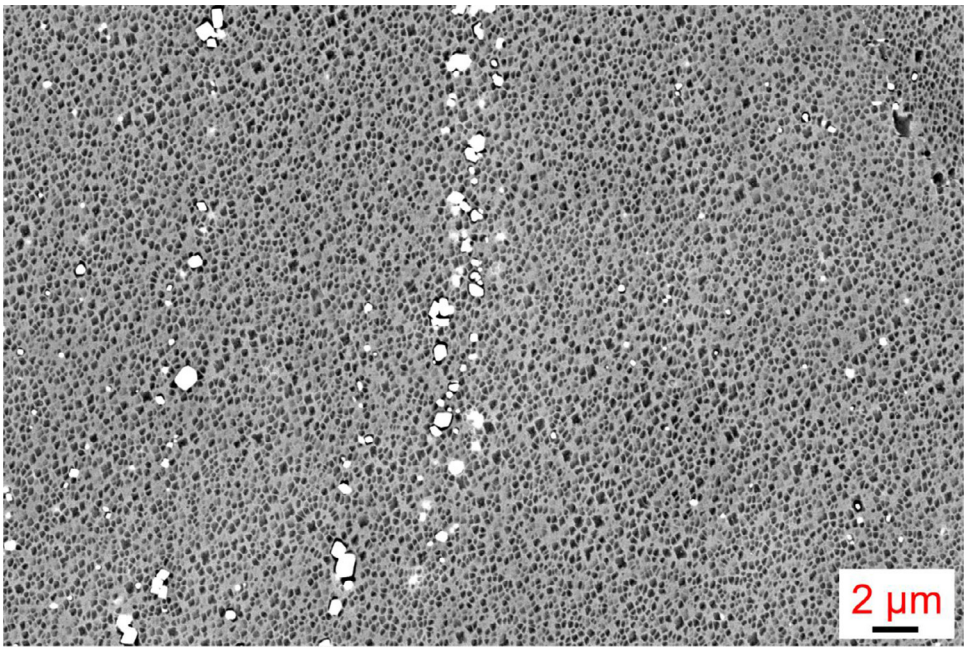

Fig. 6. Scanning electron micrograph of one of the L-PBF CM247LC alloy specimens tensile tested at 700°C showing the discrete blocky carbides (in white) and uniformly distributed γ' precipitates.

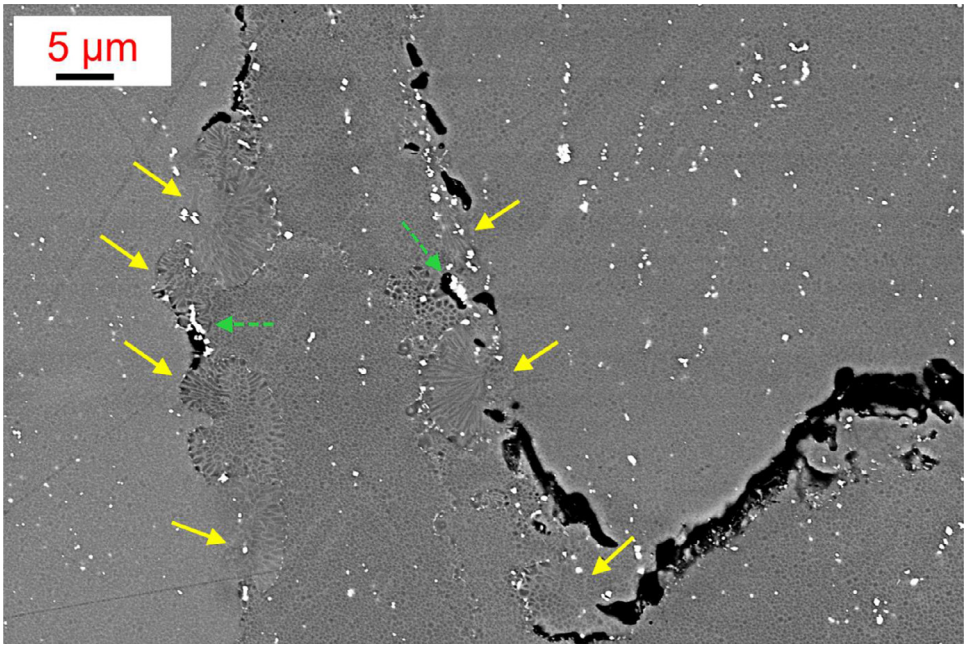

Fig. 7. Scanning electron micrograph of one of the L-PBF CM247LC alloy specimens tensile tested at 1000°C showing the agglomeration of white-coloured discrete carbides (broken arrows), microcracking and localised non-directional coarsening of γ' precipitates (solid arrows).

significantly lower than the tensile ductility (~13%) at 800°C suggesting that deformation in the considered L-PBF alloy is much more strain-rate sensitive than was expected.

It is convenient to use a time and temperature parameter like the Larson-Miller Parameter (LMP) to effectively normalise the creep rupture data acquired at different temperatures/stresses in a single plot for a given material regardless of its fabrication route. The formulation for LMP can be given as [29]:

$$\mathbf{LMP} = \left[(\mathbf{T} + \mathbf{273}) * \left(C + \mathbf{log_{10}}\ (t_\mathbf{r})\right)\right]/\mathbf{1000}$$

where T is the temperature in °C, fit constant $C = 20$ and t_r is the creep rupture time in hours. Such a plot obtained for CM247LC alloy fabricated via L-PBF, conventional casting and directional solidification is provided in Fig. 3(b). On a relative comparison, the current alloy performs better with the creep rupture time almost double at 500 MPa (assuming T = 800°C) than that for the other L-PBF CM247LC alloy reported in the literature [13]. On the other hand, the creep rupture duration for the L-PBF alloy in this work is significantly lower than that expected for the DS or CC alloys under the same test condition. Although exhibiting better tensile properties at 800°C, the creep resistance of the L-PBF alloy can thus be characterised as relatively poor compared to that for its cast or DS alloy counterparts. Improving grain size further via optimised heat treatment routine(s), grain boundary engineering and a better understanding of the precipitate/carbide evolution at elevated temperature should lead to improved creep resistance.

There is a possibility that the reported tensile and creep results could have been influenced by variations in macro/micro texture inherently associated with L-PBF builds. While the influence of texture anisotropy on mechanical properties is expected to be notably higher for as-built specimens, it is likely less pronounced as a consequence of significant

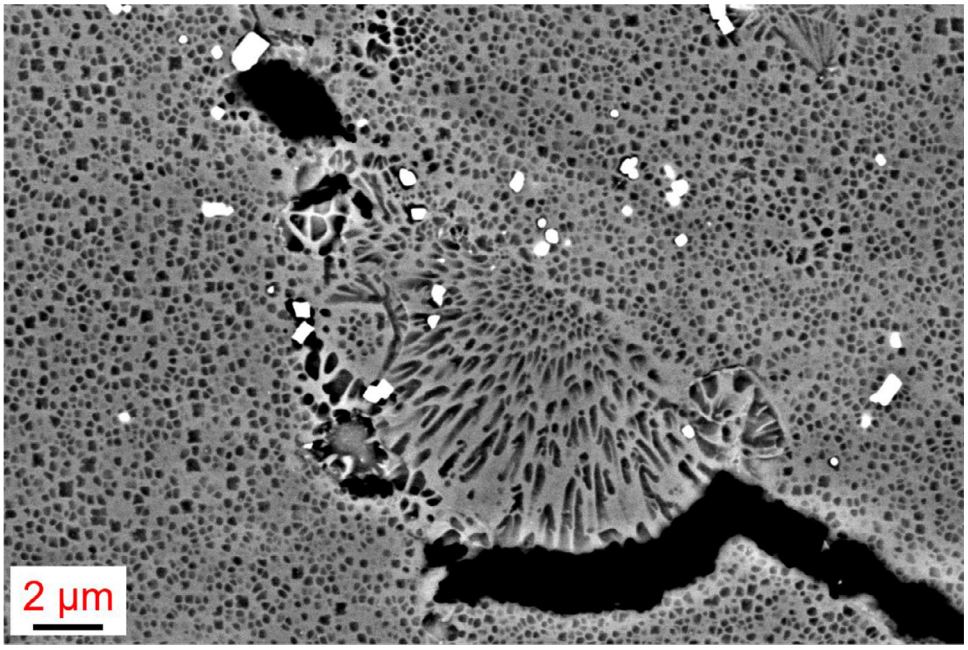

Fig. 8. Scanning electron micrograph of the 800°C, 650 MPa L-PBF CM247LC alloy creep specimen showing the non-directional localised coarsening of γ' precipitates close to the final fracture path.

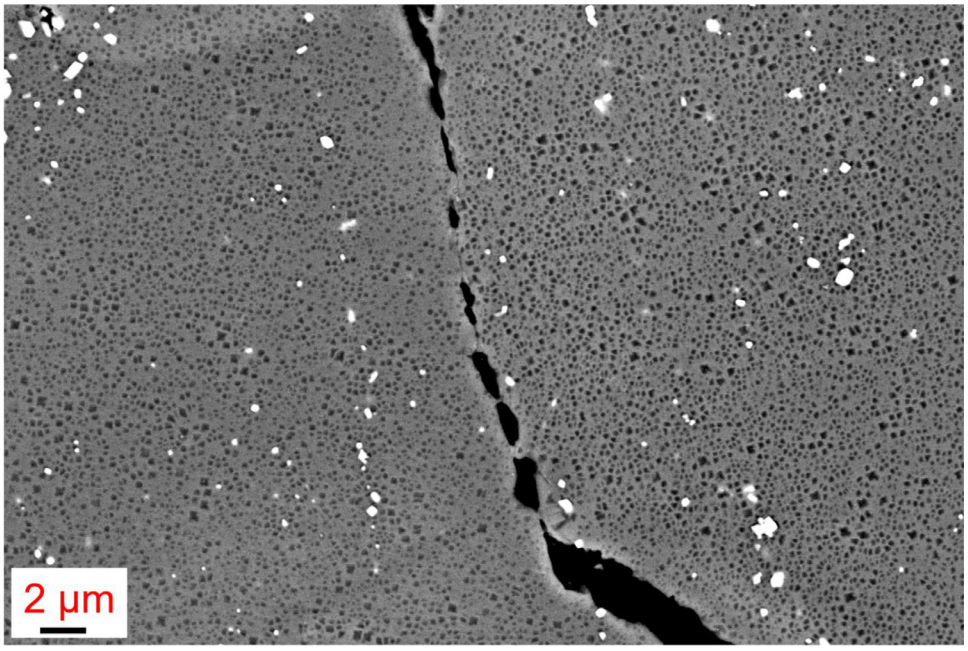

Fig. 9. Scanning electron micrograph of the 800°C, 500 MPa L-PBF CM247LC alloy creep specimen showing the linking of numerous microcracks close to the final fracture path.

recrystallisation for heat-treated high γ' volume fraction Ni-base L-PBF superalloys [15,30,31]. A more definitive statement in this context can however be made for the current alloy in consideration on the basis of dedicated X-ray Diffraction (XRD) and Electron Backscatter Diffraction (EBSD) studies as part of future work.

3.4. SEM fractography

The fracture surfaces of the creep-rupture specimens tested at 800°C under the highest and lowest applied stresses are shown in Figs. 4(a) and (b), respectively. Consistent with the very low creep ductilities noted here in Fig. 3(a), both fracture surfaces revealed a primarily intergranular mode of failure – as also observed by [28] – with instances of tortuous crack propagation. Although not evident here, neither prominent secondary cracking at the free surface nor any signs of localised necking close to the final fracture path were observed. There were, however, "pockets" of ductile features (*i.e.* voids) on the specimen tested at 500 MPa as shown for example in Fig. 4(b). Distinct flat shear facets were more obvious in the specimen creep tested at 650 MPa than that at 500 MPa.

It is well known that decohesion at triple grain junctions leads to wedge cracking as grain boundaries (GBs) oriented favourably to the applied load (in effect, local resolved shear stresses) shear/slide at elevated temperatures. Although perfectly tailored GB precipitates can greatly mitigate the propensity of the material towards grain boundary sliding, it appears not to be the case in the considered alloy at 800°C. Future studies are needed to exactly understand whether the composition and/or morphology of GB carbides need to be optimised further to enhance the creep rupture life of the alloy at temperatures ≥ 800°C. Furthermore, reducing the number density and area-fraction of GBs by increasing the grain size can also greatly assist in reducing grain bound-

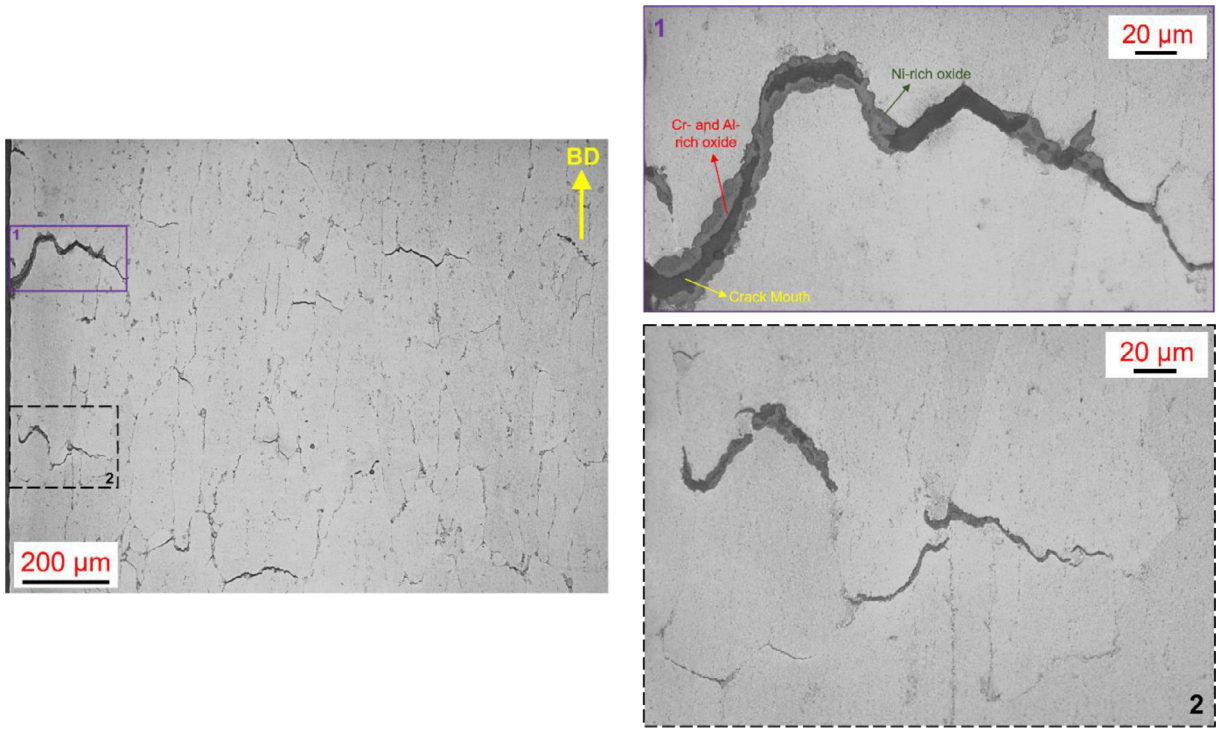

Fig. 10. Optical micrographs of the 800˚C, 650 MPa L-PBF CM247LC alloy creep specimen highlighting oxidation both at the free surface (inset 1) and at the sub-surface (inset 2).

ary sliding as shown earlier for conventionally cast CM247LC alloys in [25].

3.5. Metallographic investigation

Optical inspection of tensile specimen longitudinal sections revealed a major difference in the failure mode characteristics exhibited at RT relative to those at ET, see Fig. 5. At RT, it could be easily inferred that the material failed via transgranular mode whereas at ET, it was predominantly intergranular. All the three RT tensile specimens exhibited localised necking close to the final fracture path with negligible secondary cracking. Negligible necking with isolated instances of very short secondary free surface cracks were evident in the samples tensile tested at 700˚C. It is important to emphasise herein that no evidence of sub-surface grain boundary cracking/cavitation was apparent in the 700˚C samples except along the primary intergranular crack path. At temperatures ≥ 800˚C though, tensile samples clearly exhibited numerous instances of grain boundary cracking/cavitation with many of these microcracks linking up to the free surface especially at 1000˚C. It thus becomes apparent that GBs in the considered L-PBF alloy clearly lost their functional integrity between 700-800˚C, and crack nucleation and propagation became increasingly easier with increasing temperature.

Optical inspection of creep-rupture specimens tested at 800˚C (650 MPa and 500 MPa) reaffirmed the observations as reported in *Section 3.4*: intergranular mode of fracture with numerous instances of short secondary cracks along the test gauge length. From a macroscopic viewpoint, post-test grain sizes were not comparatively higher for both the creep specimens with those for the as-heat-treated microstructure. Considering the rupture durations (17 hours for the 650 MPa sample and 198 hours for the 500 MPa sample), it appears that short-term grain coarsening kinetics in the considered L-PBF alloy are negligible at 800˚C.

3.6. Microstructural evolution at ET

To achieve a complete characterisation of the L-PBF alloy after both tensile and creep loading, etched specimens were inspected again under the SEM with particular focus on the evolutionary aspects of precipitate and carbide structures after ET exposure. Fig. 6 shows a relatively low magnification scanning electron micrograph obtained from a sub-surface region ~2 mm below the primary crack path in the tensile specimen tested at 700˚C. Agglomeration of multiple carbides especially along a GB could be readily observed. However complete coalescence leading to a lower number density of carbides (*i.e.* carbide coarsening) was not broadly noted in this specimen. Early stages of matrix-carbide interfacial decohesion could also be observed in this figure, but was found to be more notable along the primary fracture path. Finally, no fractured carbide precipitates were found along the test gauge length indicating decohesion led microcracking to be the primary crack nucleation and propagation mechanism at 700˚C. As regards the γ' precipitates, no agglomeration or coarsening was noted. More importantly, precipitate distribution was uniform both within the grains and near the GBs.

Fig. 7 shows the typical nature of carbides and γ' precipitates near a microcrack in one of the 1000˚C tensile test specimens at ~1 mm below the primary crack path in the sub-surface region. As discussed earlier in *Section 3.5*, numerous microcracks particularly along the GBs were evident in the sample with many of the sub-surface cracks linking up to the free surface. Significant carbide coarsening was not observed, except for a few instances close to grains that did not appear to have fully recrystallised (being small in size). Agglomeration was however very prevalent and could thus greatly account for both the loss of strength and reduction in ductility at this temperature. Two instances of microcrack development aided by matrix-agglomerated carbide decohesion have been highlighted with broken arrows in this figure. The γ' precipitates, for the most part, appeared to be uniformly distributed in the microstructure and in the size distribution as for the as-heat-treated microstructure. In many regions close to GBs – especially those that had a microcrack in vicinity – the precipitates however appeared coarsened to varying extent. Several instances of localised γ' coarsening at 1000˚C have been highlighted in Fig. 7 with solid arrows (a high magnification micrograph of such γ' coarsening is provided in Fig. 8 as obtained

from an 800°C creep specimen). It is important to reemphasise that this coarsening behaviour was not directional relative to the loading axis and appeared to be more dependent on the orientation of the grains during deformation. At very high magnification, it was clear that γ' precipitates were well distributed near the GBs and hence no precipitate free zones were readily evident.

Scanning electron micrographs showing the carbide and γ' precipitate characteristics close to the final fracture path in the 800°C creep-rupture specimens tested under 650 MPa and 500 MPa stresses are presented in Figs. 8 and 9, respectively. No appreciable carbide coarsening was observed in both the cases except at isolated spots near the final fracture path in the 500 MPa specimen. Although numerous microcracks linking along GBs were present in both the specimens, the agglomeration of carbides near cracks was notably lower at 500 MPa (see Fig. 9) than that at 650 MPa (see Fig. 8). Similarly, localised γ' precipitate coarsening was more prevalent at 650 MPa than at 500 MPa (but still significantly lower than that observed at 1000°C). Both these observations possibly indicate the marked influence of local maximum resolved shear stresses (than time at a given temperature) on the aforementioned evolutionary characteristics. No carbide fracture was observed and brittle interfacial decohesion led intergranular cracking appeared to be the primary mechanism for creep rupture.

Finally, since the creep-rupture tests were conducted in ambient environment, oxidation did appear on a few of the free surface cracks (see Fig. 10 inset 1) and the thickness of oxide layers was marginally higher at 650 MPa than at 500 MPa. Except at the primary crack path, linking of sub-surface cracks to the free surface was not observed at 800°C and hence the extent of oxidation was much more site-specific. Careful analysis of all the oxidation zones indicated oxide layer formation following the intergranular crack path and no carbide dissolution was prominent in any of the adjacent regions. Preliminary Energy Dispersive X-ray Spectroscopy (EDS) studies suggested the presence of an external Ni-rich oxide followed inward by an oxide layer rich in both Cr and Al (as shown in Fig. 10 inset 1) consistent with that in the literature [32]. While oxidation was observed in limited sub-surface cracks (see Fig. 10 inset 2), the exact mechanism of oxygen transport to facilitate this behaviour is currently unclear.

Conclusions

The monotonic tensile and creep-rupture response of crack-free CM247LC alloy, processed via laser powder bed fusion, at room and at elevated temperature has been characterised in this study. The main findings can be summarised as:

1 The tensile performance of L-PBF CM247LC alloy is closely comparable to that of directionally solidified/conventionally cast material up to ~700-800°C. At further elevated temperatures up to 1000°C, reduction in both strength and ductility can be attributed to microcrack development aided by matrix-agglomerated carbide decohesion.
2 Although the creep-rupture resistance of the considered material at 800°C is comparatively better than L-PBF alloys reported in the literature, it is significantly lower than that expected for directionally solidified or conventionally cast alloys. Optimising the heat treatment strategy to further increase the grain size and improving the functional integrity of grain boundaries and discrete blocky carbides at elevated temperature can offer potential improvements in this context.
3 Creep failure at 800°C happens in a predominantly brittle intergranular mode, with metallographic evidence indicating rapid crack propagation aided by carbide-matrix decohesion especially at high stresses.
4 Although localised γ' precipitate coarsening is observed at 800°C, this microstructural evolution appears *not* to be directional relative to the loading axis and is much less prevalent than at 1000°C.
5 Finally, discrete carbide fracture or γ' denuded zones near grain boundaries are not observed for any of the tested conditions.

Declaration of Competing Interest

The authors declare that they have no known competing financial interests or personal relationships that could have appeared to influence the work reported in the article titled:

"Tensile and Creep-rupture Response of Additively Manufactured Nickel-based Superalloy CM247LC"

Yours sincerely,

Ehsan Hosseini
Dr. sc. ETH Zürich
Head of High Temperature Integrity Group (HTIG)
Experimental Continuum Mechanics
Swiss Federal Laboratories for Materials Science and Technology (Empa)
Überlandstrasse 129, CH-8600 Dübendorf, Switzerland
Email: ehsan.hosseini@empa.ch

Data Availability

Data will be made available on request.

Acknowledgements

JT and EH thank the Swiss National Science Foundation for the provided financial support (SNSF; grant number 200551).

References

[1] L.N. Carter, C. Martin, P.J. Withers, M.M. Attallah, The influence of the laser scan strategy on grain structure and cracking behaviour in SLM powder-bed fabricated nickel superalloy, J. Alloys Compd. 615 (2014) 338–347, doi:10.1016/j.jallcom.2014.06.172.
[2] X. Wang, L.N. Carter, B. Pang, M.M. Attallah, M.H. Loretto, Microstructure and yield strength of SLM-fabricated CM247LC Ni-superalloy, Acta Mater. 128 (2017) 87–95, doi:10.1016/j.actamat.2017.02.007.
[3] V.D. Divya, R. Muñoz-Moreno, O.M.D.M. Messé, J.S. Barnard, S. Baker, T. Illston, H.J. Stone, Microstructure of selective laser melted CM247LC nickel-based superalloy and its evolution through heat treatment, Mater. Charact. 114 (2016) 62–74, doi:10.1016/j.matchar.2016.02.004.
[4] M. Cloots, P.J. Uggowitzer, K. Wegener, Investigations on the microstructure and crack formation of IN738LC samples processed by selective laser melting using Gaussian and doughnut profiles, Mater. Des. 89 (2016) 770–784, doi:10.1016/j.matdes.2015.10.027.
[5] M. Ramsperger, R.F. Singer, C. Körner, Microstructure of the nickel-base superalloy CMSX-4 fabricated by selective electron beam melting, Metall. Mater. Trans. A. 47 (2016) 1469–1480, doi:10.1007/s11661-015-3300-y.
[6] L.N. Carter, M.M. Attallah, R.C. Reed, Laser powder bed fabrication of nickel-base superalloys: influence of parameters; characterisation, quantification and mitigation of cracking, in: Superalloys 2012, John Wiley & Sons, Inc., 2012, pp. 577–586, doi:10.1002/9781118516430.ch64.
[7] S. Griffiths, H. Ghasemi Tabasi, T. Ivas, X. Maeder, A. De Luca, K. Zweiacker, R. Wróbel, J. Jhabvala, R.E. Logé, C. Leinenbach, Combining alloy and process modification for micro-crack mitigation in an additively manufactured Ni-base superalloy, Addit. Manuf. 36 (2020) 101443, doi:10.1016/j.addma.2020.101443.
[8] Y.-C. Hagedorn, J. Risse, W. Meiners, N. Pirch, K. Wissenbach, R. Poprawe, Processing of nickel based superalloy MAR M-247 by means of high temperature - selective laser melting (HT - SLM), in: 2014: pp. 291–295. https://www.scopus.com/inward/record.uri?eid=2-s2.0-84892160456&partnerID=40&md5=62302042d538a33753c4a18268898c63.
[9] S. Griffiths, H. Ghasemi-Tabasi, A. De Luca, J. Pado, S.S. Joglekar, J. Jhabvala, R.E. Logé, C. Leinenbach, Influence of Hf on the heat treatment response of additively manufactured Ni-base superalloy CM247LC, Mater. Charact. 171 (2021) 110815, doi:10.1016/j.matchar.2020.110815.
[10] A. De Luca, C. Kenel, J. Pado, S.S. Joglekar, D.C. Dunand, C. Leinenbach, Thermal stability and influence of Y2O3 dispersoids on the heat treatment response of an additively manufactured ODS Ni-Cr-Al-Ti γ/γ' superalloy, J. Mater. Res. Technol. (2021), doi:10.1016/j.jmrt.2021.09.076.
[11] J.H. Boswell, D. Clark, W. Li, M.M. Attallah, Cracking during thermal post-processing of laser powder bed fabricated CM247LC Ni-superalloy, Mater. Des. 174 (2019) 107793, doi:10.1016/j.matdes.2019.107793.
[12] J.-U. Lee, Y.-K. Kim, S.-M. Seo, K.-A. Lee, Effects of hot isostatic pressing treatment on the microstructure and tensile properties of Ni-based superalloy CM247LC manufactured by selective laser melting, Mater. Sci. Eng. A. 841 (2022) 143083, doi:10.1016/j.msea.2022.143083.

[13] Y.T. Tang, C. Panwisawas, J.N. Ghoussoub, Y. Gong, J.W.G. Clark, A.A.N. Németh, D.G. McCartney, R.C. Reed, Alloys-by-design: application to new superalloys for additive manufacturing, Acta Mater. 202 (2021) 417–436, doi:10.1016/j.actamat.2020.09.023.
[14] O. Adegoke, J. Andersson, H. Brodin, R. Pederson, Review of laser powder bed fusion of gamma-prime-strengthened nickel-based superalloys, Metals 10 (2020) 996, doi:10.3390/met10080996.
[15] S. Sanchez, P. Smith, Z. Xu, G. Gaspard, C.J. Hyde, W.W. Wits, I.A. Ashcroft, H. Chen, A.T. Clare, Powder bed fusion of nickel-based superalloys: a review, Int. J. Mach. Tools Manuf. 165 (2021) 103729, doi:10.1016/j.ijmachtools.2021.103729.
[16] ASTM E8–21, Standard test methods for tension testing of metallic materialsAnnual Book of ASTM Standards, ASTM Int, West Conshohocken PA, 2021 03.01, doi:10.1520/E0008_E0008M-21.
[17] ASTM E21–20, Standard test methods for elevated temperature tension tests of metallic materialsAnnual Book of ASTM Standards, ASTM Int, West Conshohocken PA, 2020 03.01, doi:10.1520/E0021-20.
[18] ASTM E139–11, Standard test methods for conducting creep, creep-rupture, and stress-rupture tests of metallic materialsAnnual Book of ASTM Standards, ASTM Int, West Conshohocken PA, 2011 03.01, doi:10.1520/E0139-11R18.
[19] V. Paidar, D.P. Pope, V. Vitek, A theory of the anomalous yield behavior in L12 ordered alloys, Acta Metall 32 (1984) 435–448, doi:10.1016/0001-6160(84)90117-2.
[20] R.K. Rai, J.K. Sahu, P.S.M. Jena, S.K. Das, N. Paulose, C.D. Fernando, High temperature tensile deformation of a directionally solidified nickel base superalloy: Role of micro constituents, Mater. Sci. Eng. A. 705 (2017) 189–195, doi:10.1016/j.msea.2017.08.044.
[21] I.S. Kim, B.G. Choi, H.U. Hong, Y.S. Yoo, C.Y. Jo, Anomalous deformation behavior and twin formation of Ni-base superalloys at the intermediate temperatures, Mater. Sci. Eng. A. 528 (2011) 7149–7155, doi:10.1016/j.msea.2011.05.083.
[22] I.S. Kim, B.G. Choi, S.M. Seo, D.H. Kim, C.Y. Jo, Influence of heat treatment on microstructure and tensile properties of conventionally cast and directionally solidified superalloy CM247LC, Mater. Lett. 62 (2008) 1110–1113, doi:10.1016/j.matlet.2007.07.058.
[23] X. Wang, L.N. Carter, N.J.E. Adkins, K. Essa, M.M. Attallah, Novel hybrid manufacturing process of CM247LC and multi-material blisks, Micromachines 11 (2020) 492, doi:10.3390/mi11050492.
[24] J.E. MacDonald, R.H.U. Khan, M. Aristizabal, K.E.A. Essa, M.J. Lunt, M.M. Attallah, Influence of powder characteristics on the microstructure and mechanical properties of HIPped CM247LC Ni superalloy, Mater. Des. 174 (2019) 107796, doi:10.1016/j.matdes.2019.107796.
[25] H.-E. Huang, C.-H. Koo, Characteristics and Mechanical Properties of Polycrystalline CM 247 LC Superalloy Casting, Mater. Trans. 45 (2004) 562–568, doi:10.2320/matertrans.45.562.
[26] G.L. Erickson, K. Harris, R.E. Schwer, Directionally solidified DS CM 247 LC—optimized mechanical properties resulting from extensive γ' solutioning, Manuf. Mater. Metall. Ceram. Struct. Dyn. Controls Diagn. Instrum. Educ. Process Ind. 4 (1985) American Society of Mechanical Engineers, Houston, Texas, USAV004T11A006, doi:10.1115/85-GT-107.
[27] E. Balikci, R.A. Mirshams, A. Raman, Tensile Strengthening in the Nickel-Base Superalloy IN738LC, J. Mater. Eng. Perform. 9 (2000) 324–329, doi:10.1361/105994900770345999.
[28] J.N. Ghoussoub, Y.T. Tang, W.J.B. Dick-Cleland, A.A.N. Németh, Y. Gong, D.G. McCartney, A.C.F. Cocks, R.C. Reed, On the influence of alloy composition on the additive manufacturability of Ni-based superalloys, Metall. Mater. Trans. A. 53 (2022) 962–983, doi:10.1007/s11661-021-06568-z.
[29] F.R. Larson, J. Miller, A time-temperature relationship for rupture and creep stresses, Trans. ASME 74 (1952) 765–771.
[30] F. Geiger, K. Kunze, T. Etter, Tailoring the texture of IN738LC processed by selective laser melting (SLM) by specific scanning strategies, Mater. Sci. Eng. A. 661 (2016) 240–246, doi:10.1016/j.msea.2016.03.036.
[31] P. Kanagarajah, F. Brenne, T. Niendorf, H.J. Maier, Inconel 939 processed by selective laser melting: Effect of microstructure and temperature on the mechanical properties under static and cyclic loading, Mater. Sci. Eng. A. 588 (2013) 188–195, doi:10.1016/j.msea.2013.09.025.
[32] D.K. Das, V. Singh, S.V. Joshi, High temperature oxidation behaviour of directionally solidified nickel base superalloy CM–247LC, Mater. Sci. Technol. 19 (2003) 695–708, doi:10.1179/026708303225001975.